Joseph H. Solomon
Department of Mechanical Engineering,
Northwestern University,
Evanston, IL 60208,
USA

Mitra J. Z. Hartmann
Departments of Biomedical and Mechanical Engineering,
Northwestern University,
Evanston, IL 60208,
USA
m-hartmann@northwestern.edu

Extracting Object Contours with the Sweep of a Robotic Whisker Using Torque Information

Abstract

Several recent studies have investigated the problem of object feature extraction with artificial whiskers. Many of these studies have used an approach in which the whisker is rotated against the object through a small angle. Each small-angle "tap" of the whisker provides information about the radial distance between the base of the whisker and the object. By tapping at various points on the object, a full representation of the surface can be gradually constructed in three-dimensional space. It is clear, however, that this tapping method does not exploit useful information about object contours that could be extracted by "sweeping" the whisker against the object. Rotating the whisker against the object through a large angle permits the collection of a sequence of contact points as the whisker slips along the surface. The present paper derives an algorithm based on a numerical cantilever beam model of the whisker to measure object profile shape over a single large-angle whisker rotation using only information about torque and angle at the whisker base. The algorithm is validated experimentally using three different object shapes. As the method does not require measurement of force, it is well suited for implementation on an array of robotic whiskers to accomplish quick and precise object feature extraction.

KEY WORDS—whisker array, tactile perception, feature extraction, cantilever beam, biomimetic whisker, whisker slip, rat whisker system, vibrissal active touch.

The International Journal of Robotics Research
Vol. 29, No. 9, August 2010, pp. 1233–1245
DOI: 10.1177/0278364908104468

1. Introduction

Mammalian whiskers have attracted increasing interest from engineers seeking to imitate their numerous desirable sensing properties. Whiskers are physically robust, mechanically simple, and yet can precisely extract object shape, texture and the velocity of fluid flow. The diverse capabilities of whiskers are amply demonstrated by the animals that use them to perform difficult behavioral tasks; for example, seals can track hydrodynamic trails (Dehnhardt et al. 2001) and rats can distinguish small differences in aperture width (Krupa et al. 2001). Robotic whiskers have been used for various types of sensing tasks (for a review, see Solomon and Hartmann (2008)), and several recent studies have specifically addressed the issue of three-dimensional (3D) feature extraction, wherein the goal is to infer the shape of an object by repeated contact with one or more whiskers. These studies have generally taken one of two approaches: whisker tapping or whisker "sweeping".

The first approach, whisker tapping, is to rotate or translate the whisker(s) against an object by a small angle to infer where along the length of the whisker initial contact occurred (*radial distance extraction*). Using this information, along with information about the angle of initial contact and location of the whisker base, allows estimation of the contact point location in 3D space for each whisker/whisk.

Whisker tapping has been relatively well studied. Tsujimura and Yabuta (1989) derived and demonstrated a general method of estimating contact point location of a stiff probe pressing against an object using a six-axis force/torque sensor. Ueno et al. (1998) measured vibration frequencies at the base of a flexible beam using a torque sensor to estimate contact point position. Kaneko et al. (1998) used a two-axis actuator, two-axis torque sensor and a flexible beam to determine contact positions along an object based on the rotational

compliance. Clements and Rahn (2006) applied a large angle elastica model as the basis for determining contact point location with a two-axis actuator, flexible beam and six-axis force/torque sensor. Kim and Möller (2007) attached multiple flexible beams with two-axis torque sensors to an actuated support plate, showing that whisker arrays can provide basic object shape information in a single whisk. Previous work from our laboratory has shown that detailed shape information can be extracted by using a whisker array and combining data from several whisks (Solomon and Hartmann 2006), and accounting for lateral slip of the whiskers along the object (Solomon and Hartmann 2006, 2008).

The second approach, whisker sweeping, involves moving the whisker along or against the object far past the location of initial contact in order to estimate a collection of contact point locations as the whisker slips along the surface. Whisker sweeping has received less attention in the literature than tapping. Russell (1992) swept the tip of a flexible curved beam with a binary (touch or no-touch) sensor along objects with a Puma robot to measure their profile. Wilson and Chen (1995) used a pneumatic bellow tube actuation system and closed-loop control to sweep the tip of a flexible beam with a 2D torque sensor along objects and estimate their profiles. Scholz and Rahn (2004) rotated a flexible beam equipped with a six-axis force/torque load cell against objects and used a large-angle elastica model to repeatedly compute the entire whisker shape and contact point, providing an accurate 2D object profile measurement with a single whisk. Critical differences between this method and that presented here will be addressed in Section 5.

The present paper develops and demonstrates an alternative method to accomplish whisker sweeping. The method is based on incrementally inferring the change in contact point location through continuous measurement of torque (i.e. bending moment) at the whisker base. This approach was inspired by the ultimate goal of constructing a whisker array that mimics the structure of that found in the rat. This places two fundamental constraints on the system: (1) each whisker much rotate about its base, where the bending moment is measured; and (2) all whiskers must rotate in unison, thus reasonably approximating a natural whisking motion and also allowing for a simple array design that requires only a single motor for actuation (Schultz et al. 2005). Previous research in our laboratory has already established a method for performing initial contact point measurement under these conditions (Solomon and Hartmann 2008). A natural extension to these results is to develop a sweeping technique that allows continued estimation of contact point beyond initial contact, thus providing the maximum amount of available shape information per whisk.

2. Lateral Slip, Longitudinal Slip and Axial Slip

There are two distinct ways that a whisker can slip along an object. *Lateral slip* occurs when the object surface at the contact point is slanted relative to the plane of rotation and the angle of the friction cone is not large enough to prevent out-of-plane movement, as depicted in Figure 1(a) (Solomon and Hartmann 2008). Lateral slip can generate significant errors in the estimate of radial distance, and methods have therefore been devised either to prevent it from occurring by reorienting the plane of rotation (Kaneko et al. 1998; Clements and Rahn 2006), or to passively account for it (Solomon and Hartmann 2008). The latter method is most accurate when an estimate of surface friction is available. *Longitudinal slip* occurs when the curvature of the object within the plane of rotation at the contact point is finite (not a point-object or an object's corner), as depicted in Figure 1(b). Kaneko et al. (1998) showed that (in the absence of lateral slip) longitudinal slip has a small effect on radial distance extraction unless the object curvature at the contact point is very small or the contact point is very close to the base. Conveniently, longitudinal slip affords the opportunity to sense additional contact points as the whisker slips along the object periphery, providing further information about object shape over a single whisk. The algorithm presented here accomplishes this task.

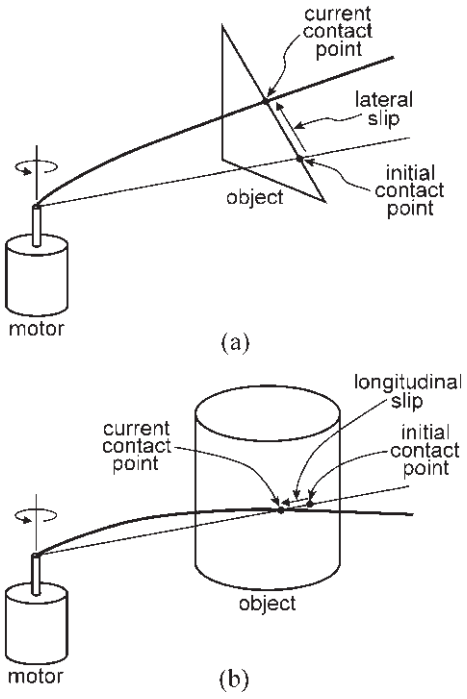

Fig. 1. There are two ways a contact point can move along an object: (a) lateral slip and (b) longitudinal slip. Note that although here they are depicted independently, they can in general occur simultaneously.

It is important to understand that the above definitions of lateral and longitudinal slip describe the movement of the contact point along the *object* in Euclidean space. The contact

point can also move along the whisker, even in the absence of lateral and/or longitudinal slip. For example, if a whisker rotates in a plane against a point object, the location of contact on the whisker will change, but the location of object contact will remain constant. This type of contact point movement on the whisker we term *axial slip*. In the analyses that follow, we are concerned primarily with longitudinal slip, as it directly determines the regions of the object being sampled.

3. Technical Approach

3.1. Determining the Initial Contact Point

We model an artificial whisker sensor typical of those used in previous studies: a thin, straight, cylindrical, flexible beam (e.g. spring steel or Nitinol wire) with a torque sensor at the base, situated to measure the beam's bending moment at its axis of rotation, which is fixed. In addition, we assume that the environment contains only static, convex objects that are rigid relative to the whisker, that the whisker bends only within its plane of rotation (no lateral slip), and that contact occurs at a discrete point along the whisker length, not at the tip. We describe methods to weaken these restrictions in Section 5.

The sensing process begins with the whisker freely rotating in the air. When a small moment threshold M_{thresh} is exceeded, indicating initial object contact, the first step is to record the current absolute whisker base angle ψ_{contact} (i.e. the encoder angle), and estimate the radial distance to the first contact point r_0, using

$$r_0 = 3EI\frac{\alpha_0}{M_0}, \tag{1}$$

where E is the Young's modulus, I is the area moment of inertia, α_0 is a small *pushing angle* (typically about 3°) beyond initial contact (where M_{thresh} is reached), and M_0 is the moment sensed in the plane of rotation at the whisker base. This equation has shown to reliably estimate radial distance with very high precision (Kaneko et al. 1998). Calculation of the contact point location in Cartesian coordinates with respect to the base is useful:

$$\begin{bmatrix} d_{x,0} \\ d_{y,0} \end{bmatrix} = \begin{bmatrix} r_0 \\ -r_0 \cdot \alpha_0 \end{bmatrix}. \tag{2}$$

Note that (2) assumes α_0 is small, so that $\sin\alpha_0 \approx \alpha_0$. Figure 2 shows the state of the whisker after measurement of the first contact point. As the whisker continues to rotate against the object, the contact point will slip along the object in a way that depends on the local shape of the object. The sweeping algorithm described in the present paper is designed to infer that local shape based on the continued measurement of torque, as outlined in the following section.

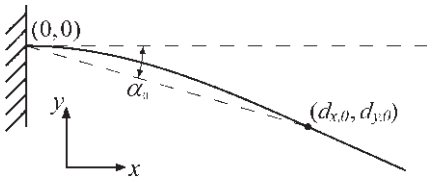

Fig. 2. Geometry of whisker after rotation by α_0. The x-axis of the local coordinate system is coincident with the line tangent to the whisker base, and the origin is at the whisker base. The magnitude of α_0 is exaggerated here, as 3° is typically sufficient.

3.2. Determining Additional Contact Points Using the Sweeping Algorithm

The basic premise of the algorithm is that given the current (iteration i, $i \geq 0$) estimated contact point location relative to the base $(d_{x,i}, d_{y,i})$ (or (r_i, θ_i) in polar coordinates), its new position after a small incremental rotation $d\alpha$ can be inferred based on the new measured moment M_{i+1}. Throughout the following derivation, it is important to note that there are two angles of interest: θ and α. The deflection angle θ is defined as the angle between the line tangent to the whisker base and the line that connects the whisker base to the current contact point, that is,

$$\theta_i = \tan^{-1}\left(\frac{-d_{y,i}}{d_{x,i}}\right),$$

where the negative sign ensures that θ is a positive quantity. The rotation angle α is the total angle that the whisker has rotated since object contact. In general, θ and α differ slightly, as depicted in Figure 3. However, in the absence of longitudinal slip, they are identical. Longitudinal slip does not occur when the contact point has infinite curvature (e.g. a point-object or the sharp corner of an object) and is negligible during the initial rotation (i.e. $\theta_0 \approx \alpha_0$) unless the object curvature at the contact point is very small and/or the contact point is very close to the base, as mentioned earlier.

The derivation begins by decomposing the translation of the contact point during a single iteration into two non-orthogonal components. The first component is a nominal deflection $\bar{\delta}_i$ tangent to the imaginary circle centered at the base and intersecting the current contact point $\left(d_{x,i}, d_{y,i}\right)$. The second component $\overline{ds}_i$ represents the longitudinal slip, occurring parallel to the longitudinal axis at the contact point (angle γ_i) and pointing towards the base. These components are depicted in Figure 4 and can be expressed as

$$\begin{bmatrix} d_{x,i+1} \\ d_{y,i+1} \end{bmatrix} = \begin{bmatrix} d_{x,i} \\ d_{y,i} \end{bmatrix} + \bar{\delta}_i + \overline{ds}_i. \tag{3}$$

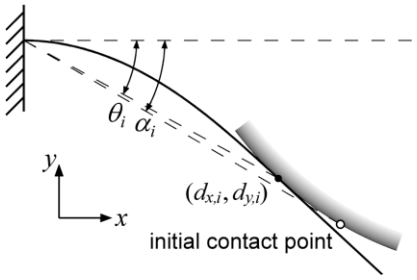

Fig. 3. Illustration of difference between α and θ. The whisker rotates by $\alpha_i = 30^\circ$ against a circle of radius 1 at an initial radial contact distance $r_0 = 1$. Because of longitudinal slip, the radial contact distance significantly decreases (becoming $r_i = 0.82$), and the deflection angle increases at a slightly slower rate than does α (becoming $\theta_i = 28.3^\circ$). These numbers were numerically generated using the method described in Appendix A.2.

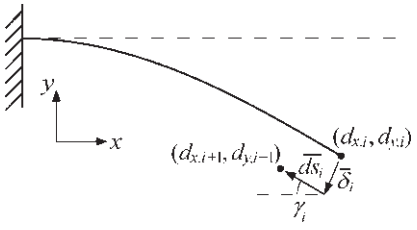

Fig. 4. Illustration of a single iteration of the sweeping algorithm. The magnitude of dα is exaggerated here, as ~1° is typically used. Negative error means that (5) yields a value smaller than numerical "ground truth."

The result of the $\bar{\delta}_i$ component is immediately evident, shifting the contact point by magnitude $r_i \cdot d\alpha$ concentric with the base, allowing us to write

$$\bar{\delta}_i = -r_i \cdot d\alpha \cdot \begin{bmatrix} \sin\theta_i \\ \cos\theta_i \end{bmatrix}. \tag{4}$$

Finding the direction and magnitude of $\overline{ds_i}$ is more difficult. These two problems will now be treated independently.

As stated earlier, $\overline{ds_i}$ is oriented parallel to the longitudinal axis of the whisker at the contact point, at contact angle γ_i. For small θ, it is straightforward to show using Euler–Bernoulli beam theory applied to the classical model of a cantilever beam with concentrated end load, that

$$\gamma \approx \frac{3}{2}\theta \tag{5}$$

for small deflections (see Appendix A.1). However, assumptions of linearity are violated for angles larger than about 10°, and hence we turn to a numerical elastica model to compute the relation between γ and θ for larger deflections.

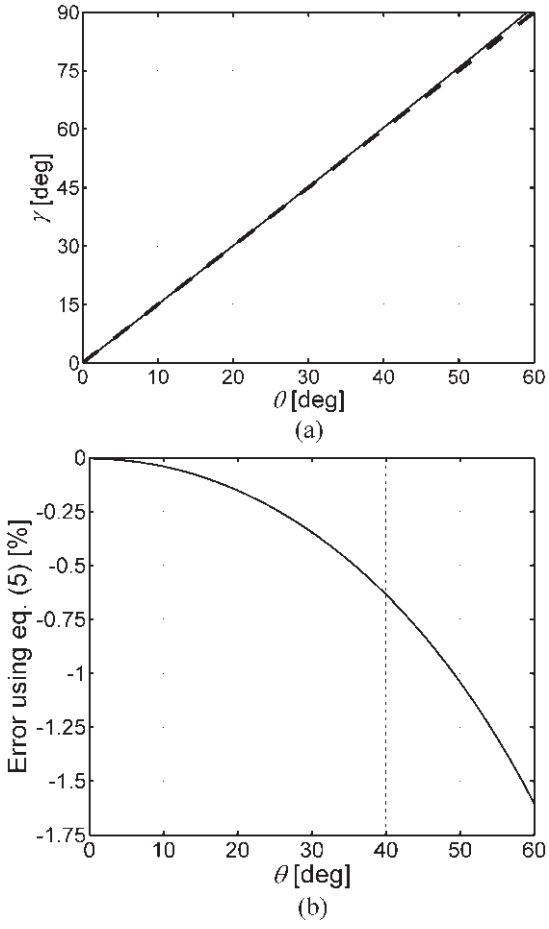

Fig. 5. Deflection angle analysis. (a) Relationship between contact angle γ and deflection angle θ for a cantilever beam with concentrated end load. The solid line is the numerical result, and the dashed line is from (5). (b) Error incurred using (5) as a function of θ.

The model considers a static cantilever beam divided into n nodes, with a concentrated load F at arc length $s_F = 1$ along the beam. Friction is assumed to be zero, and the force therefore acts perpendicular to the longitudinal axis at the force location. Starting at node 1 where the force is applied, the shape of the beam is iteratively computed node-by-node towards node n at the base using a version of the Euler–Bernoulli equation. Repeating this procedure for a range of forces provides a sequence of beam shapes for increasingly large deflections, with units automatically normalized by E, I and s_F. The resulting table can be efficiently interpolated to generate the beam shape, curvature or moment at the base, and contact angle γ for various methods of query, including (d_x, d_y), (r, θ), and (s_F, F, EI). Details can be found in Appendix A.2.

Using the results of the numerical model, Figure 5(a) plots γ versus θ for up to $\theta = 60^\circ$. Perhaps surprisingly, Equa-

tion (5) continues to hold with very high accuracy well past the regime where small angle assumptions are valid. Figure 5(b) shows that use of (5) results in only –0.35% error at $\theta = 30°$, and –1.63% error at $\theta = 60°$. Since sweeps of less than 60° are likely to be used in practice, Equation (5) is a very good approximation even for large angles and thus is used to estimate the orientation of $\overline{ds}_i$.

The only remaining task is to formulate a method of estimating $|ds_i|$, the magnitude of $\overline{ds}_i$, which (neglecting friction) depends entirely on the curvature of the object surface at the current contact point. If the curvature is infinite (i.e., the contact point is the corner of an object or a point-object), then $|ds_i| = 0$; otherwise, $|ds_i| > 0$. To estimate $|ds_i|$ when it is non-zero, we express it as a function of the new moment at the whisker base M_{i+1}, as well as two numerically computed quantities.

Defining $M_{\delta,i}$ as the moment after deflection δ_i and $\mathrm{d}M_i/\mathrm{d}s$ as the rate of change of moment with respect to $|ds_i|$ (following along the beam towards the base) we can write

$$M_{i+1} = M_{\delta,i} + \frac{\mathrm{d}M_i}{\mathrm{d}s} \cdot |ds_i| \,. \tag{6}$$

Solving for $|ds_i|$, we have

$$|ds_i| = \left(M_{i+1} - M_{\delta,i}\right) \cdot \frac{\mathrm{d}s}{\mathrm{d}M_i}. \tag{7}$$

Consolidating (5) and (7),

$$\overline{ds}_i = \left(M_{i+1} - M_{\delta,i}\right) \cdot \frac{\mathrm{d}s}{\mathrm{d}M_i} \cdot \begin{bmatrix} -\cos\left(\frac{3}{2}\theta_i\right) \\ \sin\left(\frac{3}{2}\theta_i\right) \end{bmatrix}. \tag{8}$$

Finally, combining (3), (4) and (8), we have

$$\begin{bmatrix} d_{x,i+1} \\ d_{y,i+1} \end{bmatrix} = \begin{bmatrix} d_{x,i} \\ d_{y,i} \end{bmatrix} - r_i \cdot d\alpha \cdot \begin{bmatrix} \sin\theta_i \\ \cos\theta_i \end{bmatrix} + \left(M_{i+1} - M_{\delta,i}\right) \cdot \frac{\mathrm{d}s}{\mathrm{d}M_i} \cdot \begin{bmatrix} -\cos\left(\frac{3}{2}\theta_i\right) \\ \sin\left(\frac{3}{2}\theta_i\right) \end{bmatrix}. \tag{9}$$

As M_{i+1} is measured by the torque sensor, there are only two remaining unknown variables needed to find the new contact point: $M_{\delta,i}$ and $\mathrm{d}M_i/\mathrm{d}s$. Again, the numerical model provided in Appendix A.2 is used, and the results are shown in Figure 6. The curves are normalized using r as a scaling parameter, so that M_δ has units of $[EI/r]$, and $\mathrm{d}M/\mathrm{d}s$ has units of $[EI/r^2]$. Also shown are the results of cubic polynomial fits to both curves (dashed lines), which serve as convenient methods of implementing these relations. The polynomials contain no degree-zero term since the underlying function passes through

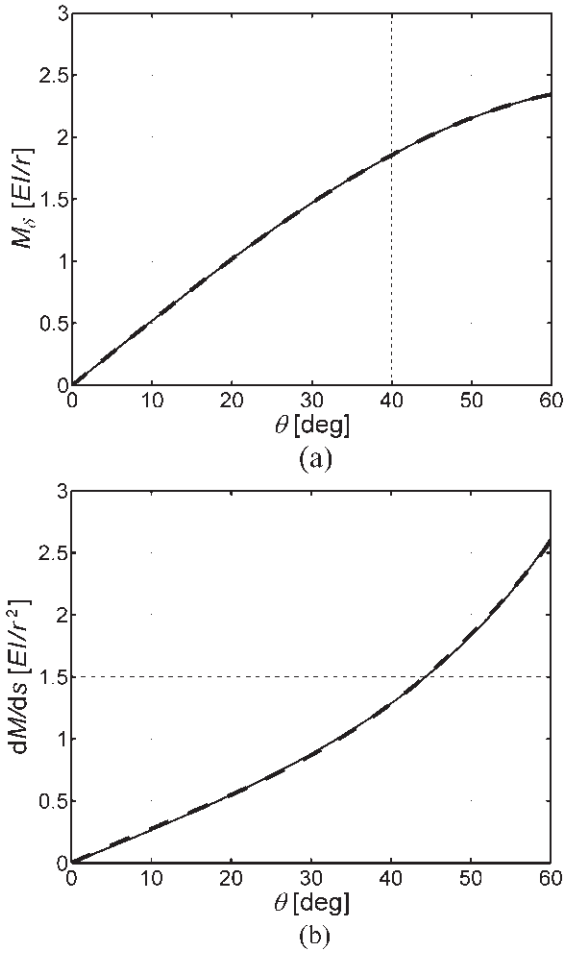

Fig. 6. Relationships between moment and deflection angle used by the sweeping algorithm: (a) M_δ versus θ; (b) $\mathrm{d}M/\mathrm{d}s$ versus θ. The solid lines are the numerical data, and the dashed lines are cubic polynomial fits to the data. See Appendix A.2 for details of the numerical model.

the origin, and were fit by minimizing the sum of squared errors. The resulting equations are as follows:

$$M_{\delta,i} = \frac{EI}{r_i} \cdot \left(-0.6673 \cdot \theta_i^3 - 0.0354 \cdot \theta_i^2 + 3.0069 \cdot \theta_i\right). \tag{10}$$

$$\frac{\mathrm{d}M_i}{\mathrm{d}s} = \frac{EI}{r_i^2} \cdot \left(1.5289 \cdot \theta_i^3 - 0.8402 \cdot \theta_i^2 + 1.6799 \cdot \theta_i\right). \tag{11}$$

where θ_i is in units of radians and $r_i = \sqrt{d_{x,i}^2 + d_{y,i}^2}$. Note that (10) and (11) have the relevant normalization factors included, but also that the bending stiffness EI may not be obtainable

with high precision. In practice, it is not necessary to know EI, as the torque sensor is calibrated to units of curvature at the whisker base (e.g. from voltage), in which case EI effectively becomes unity. This is addressed further in Section 4.

At each step of the algorithm, the current contact point is computed with respect to the current local (x-y) reference frame. Therefore, conversion to coordinates in a global (X-Y) reference frame is necessary. This is straightforward using a rotation matrix:

$$\begin{bmatrix} d_{X,i} \\ d_{Y,i} \end{bmatrix} = \begin{bmatrix} \cos\psi_i & \sin\psi_i \\ -\sin\psi_i & \cos\psi_i \end{bmatrix} \begin{bmatrix} d_{x,i} \\ d_{y,i} \end{bmatrix}, \qquad (12)$$

where $\psi_i = \psi_{\text{contact}} + \alpha_i$, and is the angle tangent to the whisker base in the global coordinate system.

Before testing the sweeping algorithm in hardware, it was validated numerically by simulating the rotation of a cantilever beam against circles of varying diameter and at varying distances. The beam shapes and moments at the base were computed using the numerical model in Appendix A.2. Using $\alpha_0 = 3^\circ$ and $d\alpha = 1^\circ$, the extracted contact points aligned nearly perfectly along the circles' perimeters. As expected, the smaller α_0 and $d\alpha$ were scaled, the closer the alignment between contact points and surface.

For completeness, we note that in certain applications, the whisker may need to be linearly translated instead of rotated against the object. Modification of the algorithm for translation is straightforward, and is included in Appendix A.3.

4. Experimental Results

The algorithm was tested using aluminum bars with circular-, hexagonal- and square-shaped cross sections. The robotic whisker used in these experiments has been used in previous research (Solomon and Hartmann 2006, 2008). Typical of robotic whisker designs, it consists of a straight, flexible wire to act as the vibrissa, attached to a torque sensor at the base (the "follicle"). The vibrissa is 0.5 mm in diameter and 5 cm in length, and composed of superelastic Nitinol ($E \approx 80{,}000$ MPa) to ensure retention of its original straight shape. The follicle is a small aluminum block (4 × 4 × 8 mm) with a strain gage attached to each of its four exposed faces. Although the follicle is capable of sensing both orthogonal components of moment, no lateral slip occurred in these experiments and hence only two of the four strain gages were used. The follicle was attached to an aluminum bar with a set screw, and the bar was attached to an AC servomotor for actuation. The base of the vibrissa (and tip of the follicle) resides at the resulting axis of rotation, ensuring adherence to the sensing model. The centers of the test objects were placed 4 cm in front of the whisker base, as shown in Figure 7.

Before experimental data were taken, calibration trials were performed to convert the strain gage voltage output to curvature at the whisker base. Curvature and moment are linearly related by the bending stiffness EI (see (19)). In practice, it is more convenient to calibrate the follicle to curvature instead of moment since knowledge of E and I is not required. All experimental and calibration data were low-pass filtered at 800 Hz, sampled at 2,000 Hz, and passed through a zero-phase digital filter with a cutoff frequency of 10 Hz.

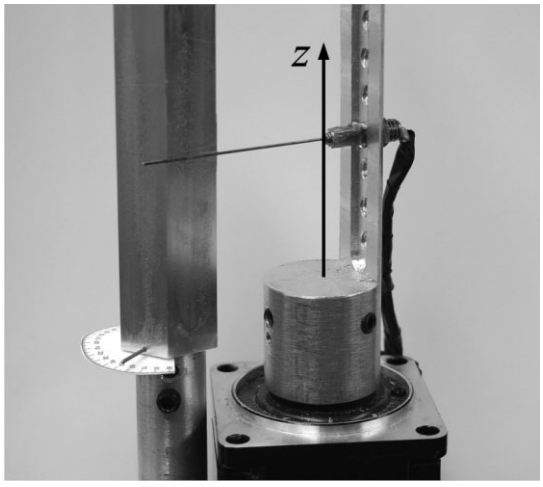

Fig. 7. The experimental setup. The whisker was rotated against aluminum bars with circular-, hexagonal- and square-shaped cross sections (hexagonal shown here). The vertical arrow indicates the axis of rotation. The protractor shown underneath the object was used to manually set its orientation.

The follicle was calibrated by rotating the whisker at a speed of $10^\circ\ s^{-1}$ through an amplitude of 60° against a slender peg at a radial distance of 4 cm (starting out barely touching). Using (10) with EI set to 1 allows the true curvature to be inferred for all values of θ. Plotting curvature versus voltage generates a calibration curve, which was stored as a cubic spline, to be used to convert the experimental data from voltage to curvature. The curve starts out linear, but levels off slightly as the curvature becomes large.

Each experimental trial occurred as follows. The whisker started at rest, placed at a radial distance of 4 cm and oriented -30° relative to the object's center. At a speed of $10^\circ\ s^{-1}$, the whisker was rotated against the object with an amplitude of 60°, immediately retracting back to -30°. The whisker was held stationary while the object was rotated about its center by 30°. This procedure was repeated an additional 11 times, resulting in the whisker contacting all or almost all of the objects' perimeters. Although in actuality we are keeping the location of the whisker base fixed in space and rotating the object between whisks, this is functionally equivalent to having the whisker base move around the fixed object between whisks, in a circular manner.

After filtering the data, Equations (1) and (2) were used to compute the initial contact point using $\alpha_0 = 3^\circ$. Subsequent

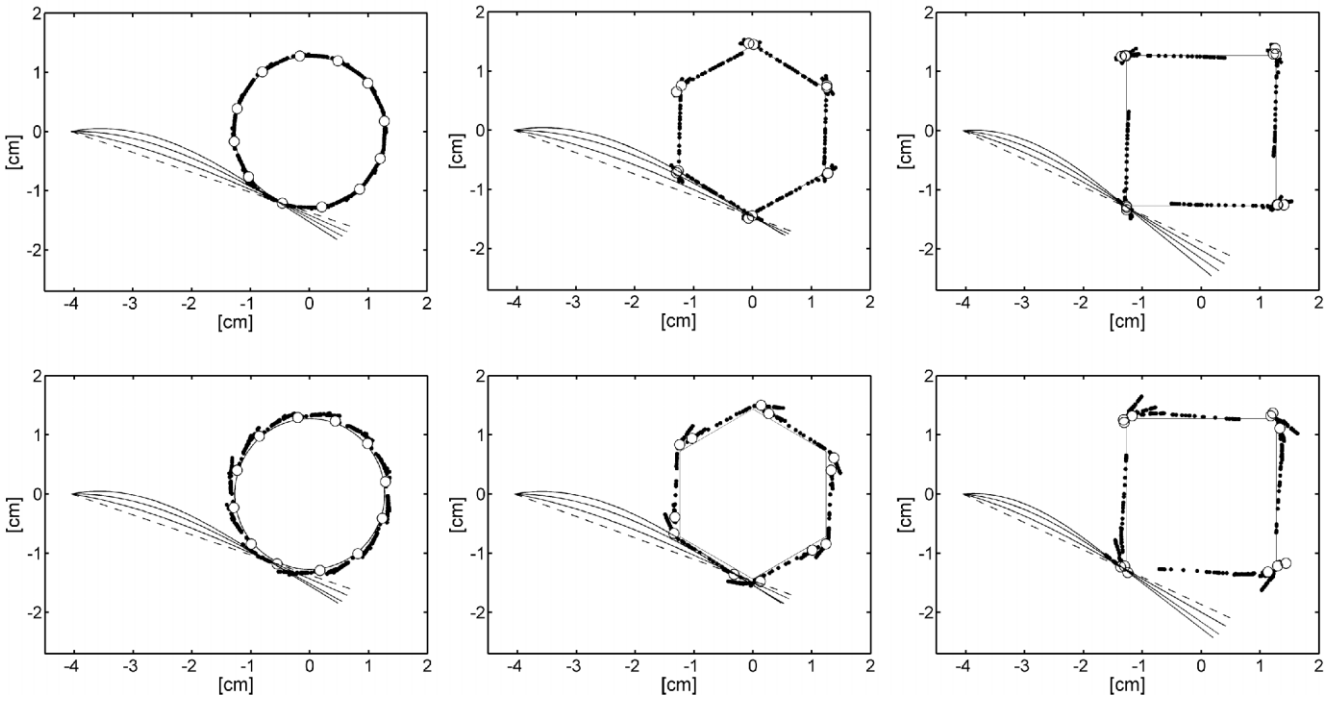

Fig. 8. Results of implementing the sweeping algorithm on smooth and rough objects. Top row: sweeping results for objects with a smooth surface. Bottom row: sweeping results for rough objects (covered in 120 grit sandpaper). A total of 12 whisks were performed at evenly spaced (30°) intervals around the objects. Initial contact points are indicated by small white circles and subsequent points computed by the sweeping algorithm are indicated by smaller black dots. Thin lines indicate the actual underlying shape profile. For the first whisk, the orientation of the whisker upon object contact is indicated by the dashed line, and subsequent whisker shapes are indicated in 10° increments by solid lines. These shapes were generated using the numerical model in Appendix A.2. This was done for illustrative proposes only. Calculation of the full whisker shape at each time step is not required by the sweeping algorithm presented here.

points were generated by iteratively applying (9)–(11), with $d\alpha = 1^\circ$. This procedure gives the contact points within the local whisker reference frame (see Figure 3); hence conversion to a global frame using (12) was necessary before plotting. The results, shown in the top row of Figure 8, demonstrate that the sweeping algorithm accurately estimates successive contact points as the whisker slips along the perimeters of all three shapes.

The sweeping algorithm assumes no friction between the whisker and the object, which influences (5), (10) and (11). These equations were derived under the assumption that the direction of the contact force is normal to the whisker at the contact point, which is increasingly inaccurate for a rough object as θ becomes large. To test the effect of friction, the experiments were repeated with 120 grit (moderately rough) adhesive-backed sandpaper stuck to the objects. The bottom row of Figure 8 shows that although some precision is lost, the general object profile shapes are again faithfully reproduced. Increasing the friction further would likely result in increasingly inaccurate results, but such rough objects are unlikely to be encountered in most applications.

Another important parameter is the whisking speed. The experiments described here used a slow speed ($10^\circ\ s^{-1}$) to minimize inertial effects, but much faster speeds can be implemented in practice. The above experiments were repeated using a whisking speed of $90^\circ\ s^{-1}$ with similar results for both smooth and rough surfaces (data not shown). Qualitatively, the only significant difference involved a greater dispersion of contact points at the edges of the smooth objects. Increasing the whisking speed significantly beyond about $90^\circ\ s^{-1}$ should be done with caution, as inertial effects will increasingly generate torque signals at the base. Possible methods to mitigate inertial effects might include insuring smoothness of the actuation trajectory, e.g. by integrating some form of machine learning component with the algorithm.

To give a quantitative measure of contact point extraction accuracy, ideally we would have measured the distance from each estimated contact point to its actual contact point, but do-

Table 1. Quantification of Estimated Contact Point Accuracy

Experimental conditions	Average error (mm)	Average normalized error (%)
Smooth surface, $\dot{\alpha} = 10^\circ\ s^{-1}$	0.32	0.85
Rough surface, $\dot{\alpha} = 10^\circ\ s^{-1}$	0.88	2.39
Smooth surface, $\dot{\alpha} = 90^\circ\ s^{-1}$	0.35	0.92
Rough surface, $\dot{\alpha} = 90^\circ\ s^{-1}$	0.52	1.41

ing so would have required use of a high-speed video camera and cumbersome image analysis. Instead, the error associated with each contact point was defined as the minimum distance from the point to the object surface. The error was also computed in a normalized form by dividing the absolute error by the initial contact distance r_0 for each whisk. Table 1 presents these results for each of the four experimental conditions, each averaged over all three shapes. Consistent with Figure 8, the rough surface condition decreases the overall accuracy, but average error remains under 1 mm (2.39%). Table 1 also confirms that whisking at $90^\circ\ s^{-1}$ does not significantly affect the results.

5. Discussion

The sweeping algorithm presented here has been shown to be highly accurate for three distinct two-dimensional shapes. In all three cases, the entire profile shape was reliably extracted with only 12 whisks, clearly providing significant additional shape information beyond the initial contact point alone. In addition, visual inspection showed that the sequence of extracted points closely matched the actual movement of the whisker along the object. In several cases, the whisker remained in discrete contact with a corner during an entire whisk (zero longitudinal slip). As expected, the estimated contact points would remain in the same region, usually within a range of 2 mm from the first contact point for the smooth objects (but up to about 5 mm for rough objects). In other cases, significant slip along the object occurred, whereupon the estimated contact point would accurately align with the perimeter of the object.

The sweeping algorithm described here requires reasonable choices to be made for M_{thresh}, α_0 and $d\alpha$. Here M_{thresh} should be as close to zero as possible while ensuring it is not exceeded as a result of dynamic effects and sensor noise. A good rule of thumb is to make α_0 as small as possible, while still ensuring a strong enough torque signal to allow accurate distance extraction when contact occurs near the whisker tip. The choice of $d\alpha$ is predicated on a tradeoff between accuracy and computational efficiency, as well as the desired number of extracted points. Efficiency will generally be a negligible issue, as each iteration involves only evaluating the algebraic equations (9)–(12). However, decreasing $d\alpha$ below 1° typically has an insignificant effect on the accuracy of the algorithm. (In fact, reasonable accuracy can be obtained for $d\alpha$ as large as $\sim 5^\circ$.) Therefore, in general practice, a choice of $d\alpha$ is determined by the desired number of extracted contact points.

The assumptions inherent in the sweeping algorithm deserve careful consideration.

- *Friction*. Although the assumption of zero friction is not technically valid if the surface is rough, we have shown that the sweeping algorithm produces good results even in the relatively extreme case of 120 grit sandpaper. The model has thus been empirically shown to work in the presence of friction, albeit with somewhat reduced accuracy.

- *Tip contact*. For distance extraction with (1), tip contact is easily handled by setting an upper threshold on r_0 equal to the length of the whisker (Solomon and Hartmann 2006). However, the assumption that the contact force acts normal to the whisker at the contact point can be inaccurate if the whisker touches the object at the tip, and also the tip can slide along the object, invalidating (4). We implemented a modified version of the sweeping algorithm for the case of tip contact, setting $\overline{ds}_i$ to zero (since tip contact generally persists during a whisk), and using a numerical technique to estimate $\bar{\delta}_i$ based on the moment M_{i+1}. Unsatisfactory results were obtained. Therefore, in practice, the sweeping algorithm should be halted for whisks in which, during the initial "tap" of the whisker on the object, r_0 is found to be equal to the whisker length, and the location of the whisker base moved closer to ensure contact along the whisker length.

- *Lateral slip*. The sweeping algorithm explicitly assumes that no lateral slip occurs; any significant amount is likely to be highly detrimental. Note that this does not necessarily require that the surface be oriented exactly perpendicular to the plane of rotation, as friction can prevent lateral slip in some cases (Solomon and Hartmann 2008). When lateral slip does occur, it can easily be sensed through measurement of the orthogonal (y) component of moment, in which case either the sweeping algorithm could be halted until the next whisk, or the plane of rotation could be actively adjusted to prevent lateral slip from occurring (Kaneko et al. 1998; Clements and Rahn 2006).

- *Concave object features*. Two situations must be addressed.

    1. If the whisker contacts the object at two discrete points during its initial rotation by α_0, then

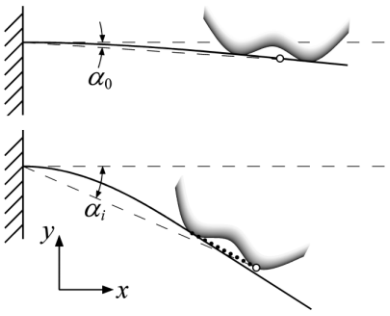

Fig. 9. Possible problems associated with concave object features. In the statistically unlikely event that the whisker contacts the object at two discrete points during its initial rotation α_0 (top), the estimated contact point (white circle) will reside somewhere between the two actual contact points. Another possible problem may occur when a concave object feature causes the whisker to contact the object at two discrete points during the sweep (bottom), in which case extracted contact points (black dots) will align the region between the actual contact points.

distance extraction using (1) can be affected, as shown in the top part of Figure 9. However, this situation is statistically unlikely to occur because it would require two points along the object to precisely align with the whisker upon contact. Regardless, it is relevant to note that our empirical results demonstrated that the sweeping algorithm is able to quickly "damp out" error associated with the use of (1). To show this, we processed the experimental data, except that r_0 was set to random values between zero and the whisker length, instead of using (1). After an additional rotation of about 5–10° (depending on the error in r_0), subsequent extracted points aligned accurately along the objects. This inherent robustness can be explained by the iterative nature of the algorithm. When r_0 is inaccurate, the $|ds_i|$ component of (9) (see also (6)) will cause the estimated contact point location to move increasingly close to actual contact point following each iteration.

2. Concave regions of an object might be omitted ("swept over") as the whisker rotates through a large angle, in which case the sweeping algorithm would effectively place contact points along the line connecting those parts of the object that were actually touched, as shown in the bottom part Figure 9. In order to subsequently discover such a concave feature, the base of the whisker would have to be translated to a new location such that the whisker tip crosses the line of false contact points, thus indicating their inaccuracy and allowing them to be discarded. Note that for a straight whisker, it is geometrically possible to sample concave object features only through contact at the whisker tip.

- *Non-discrete object contact.* During a whisker sweep, the whisker may come into contact with the object along a continuous segment of its length, inconsistent with the discrete contact model. This situation clearly occurred in the experiments for both the hexagon and square objects, yet it did not adversely affect the results. This form of robustness is a result of the mechanical nature of segmental object contact, which produces a moment at the base equivalent to discrete object contact at some point within the same segment. Thus, in such cases, the algorithm will effectively determine the contact point to be somewhere along the contact segment.

- *Object compliance*. If the object is not rigid relative to the stiffness of the robotic whisker(s), computation of r_0 using (1) and the $\bar{\delta}_i$ components using (4) during a sweep may be inaccurate. A method for finding r_0 for a compliant object is offered by Kaneko et al. (1998) which involves whisking at two different distances. Although further research would be required to accommodate the sweeping algorithm, the most straightforward solution is to use thin, flexible robotic whiskers so that the compliance of most objects is negligible compared with that of the whisker. The benefit of decreasing whisker stiffness must be balanced against the drawback of decreasing the torques that will be sensed. As a rule of thumb, the stiffness should be large enough to ensure a sufficient reaction torque after rotating by α_0 to allow accurate use of (1) in the case that the whisker touches the object near its tip. Note that $I = \frac{1}{4}\pi r^4$, so that halving the whisker diameter will decrease I (i.e. stiffness) by a factor of 16.

- *Moving objects.* As the algorithm assumes that the object is static, any change in sensed moment due to movement of the object will be wrongly interpreted. The most straightforward solution is to whisk at a speed which nullifies object movement. As real rat whiskers have very little mass, they move very rapidly (up to 1500° s^{-1} (Towal and Hartmann 2008)).

It is interesting to compare the sweeping algorithm developed here with that implemented by Scholz and Rahn (2004). Scholz and Rahn use a hub load cell and a non-linear elastica model to numerically integrate the shape of the whisker at each time step. One advantage of this approach is that it does not lose accuracy when contact occurs at the tip. Another possible advantage is that active movement of the whisker is not explicitly required; in other words, the base angle, force and

torque history over a given sweep are not needed to estimate a given contact point. However, there are two drawbacks to their method. The primary drawback is that it requires a sensor that can measure two components of force in addition to moment. These load-cell sensors are typically prohibitively bulky and expensive for use in an array of whiskers. In contrast, the parts to construct the torque sensor used in this study only cost about US$20 (four strain gages, only two of which were used); see Solomon and Hartmann (2008). The second drawback is that the technique involved numerically computing the shape of the whisker each time step, which can require significant computational resources to run in real time for multiple whiskers. In contrast, the algorithm presented here computes contact points by iteratively inferring position changes based on small successive changes in whisker angle α and sensed moment M. This makes it extremely efficient, involving only the evaluation of the algebraic equations (9)–(12) on each iteration. It should be noted, however, that the computational efficiency of Scholz and Rahn's method could be improved by pre-solving their elastica model for a range of deflections, and storing the results in a three-dimensional lookup table, which could then be interpolated to compute each contact point.

Although our method has been derived for cylindrically-shaped whiskers, it is not limited to this case. Real rat whiskers are tapered (roughly linearly with respect to arc length) and curved (Solomon and Hartmann 2006), and it is interesting to ask whether the sweeping algorithm could work for a whisker with these geometrical characteristics. Theoretically, the answer is yes. Equation (1) would simply be replaced with the distance extraction equation for a curved, conical whisker (Solomon and Hartmann 2006). However, γ, M_δ and $\mathrm{d}M/\mathrm{d}s$ would now also depend on the arc length contact distance s_F in addition to θ. As a result, (5), (10) and (11) would become functions of two variables, θ and s_F. These functions could be generated using the numerical method in Appendix A.2 and stored in a look-up table (or any convenient function approximator, e.g. two-variable polynomial, radial basis function network, or multilayer perceptron). Equations (8) and (9) would also change in accordance with (5).

Future research is needed to develop a strategy for dealing with tip contact. Another interesting possibility is to expand the algorithm to allow continued estimation of contact point location during lateral slip. Other recent work from our laboratory has addressed the problem of accurate distance extraction in the presence of lateral slip (Solomon and Hartmann 2008), so much of the puzzle has already been addressed. The development of such a three-dimensional version of the sweeping algorithm described here that incorporates a two-dimensional torque sensor would be of great benefit to the ultimate goal of quick and precise object feature extraction with a robotic whisker array.

6. Conclusion

In this paper we have derived and demonstrated an effective, efficient and easy-to-implement method for obtaining object profile shape information over a single whisk with a robotic whisker. As force does not need to be measured, the physical implementation of the algorithm requires only small, inexpensive torque sensors (e.g. strain gages). This makes it easy to implement on a highly parallel array of robotic whiskers. The algorithm was shown to be robust to sensor noise, object friction and segmental contact.

The extraction of a continuous segment of an object's profile with a single whisker/whisk is also somewhat biologically plausible. For example, a rat could extract the contour of an object from torque information measured at the base of each of its tapered whiskers. In fact, the taper of the whisker would serve to increase the length of the object contour swept over, as the whisker would increasingly tend to bend in on itself for contact near the tip. Although "sensor noise" would be a significant limiting factor in the rat, it is possible that basic curvature information could be extracted.

Acknowledgment

This work was supported by NSF awards IOB-0446391 and IIS-0613568 to MJZH.

Appendix

A.1. Derivation of the Relationship Between γ and θ

Application of linear elasticity to small angle deflections of a cantilever beam shows that the deflected shape owing to a concentrated end load F can be expressed as

$$y(x) = \left(\frac{F}{6EI}\right)\left(3x^2 d_x - x^3\right) \tag{13}$$

and the slope is given by

$$\frac{\mathrm{d}y}{\mathrm{d}x} = \left(\frac{F}{6EI}\right)\left(6x d_x - 3x^2\right). \tag{14}$$

Evaluating (13) and (14) at $x = d_x$, we have

$$y(d_x) = d_y = \left(\frac{F d_x^3}{3EI}\right) \tag{15}$$

and

$$\left.\frac{\mathrm{d}y}{\mathrm{d}x}\right|_{d_x} = \left(\frac{F d_x^2}{2EI}\right). \tag{16}$$

We also know that

$$\tan\theta = \left(\frac{-d_y}{d_x}\right) \quad \text{and} \quad \tan\gamma = \left.\frac{-\mathrm{d}y}{\mathrm{d}x}\right|_{d_x}.$$

Using these equations along with (15) and (16) gives us

$$\tan\theta = \left(\frac{-Fd_x^2}{3EI}\right) \tag{17}$$

and

$$\tan\gamma = \left(\frac{-Fd_x^2}{2EI}\right). \tag{18}$$

For small angles, $\tan\theta \approx \theta$ and $\tan\gamma \approx \gamma$, leading to Equation (5):

$$\gamma \approx \frac{3}{2}\theta.$$

A.2. Determining the Shape of a Cantilever Beam for Large Deflections

The problem of determining the shape of a cantilever beam subjected to a point load at the end is one of the oldest in the study of bending beams, having been investigated by Bernoulli and Euler in the 1700s. Precise solutions can be obtained through the use of elliptic functions (Landau and Lifshitz 1986), and recent methods allow the determination of all equilibrium shapes, given material and geometric properties and end load (Navee and Elling 1992; Batista and Kosel 2005). Here, we are interested only in determining a small subset of possible equilibrium shapes, namely those that can be expected to arise during a whisker rotation of reasonable amplitude against on object. It is assumed that dynamic effects are negligible, allowing use of a standard elastic model of beam bending.

The Euler–Bernoulli beam equation can be written as

$$\mathrm{d}\kappa = \frac{M}{EI}, \tag{19}$$

where $\mathrm{d}\kappa$ represents change in curvature, and can vary with M, E and I along the length of the beam. Computation of the shape of a cantilever beam for an end load of arbitrary magnitude and direction can be accomplished by dividing the beam into n nodes and writing (19) in the following form:

$$\mathrm{d}\kappa_i = \frac{\mathrm{d}\phi_i}{\mathrm{d}s} = \frac{\bar{r}_i \times \overline{F}}{E_i I_i} \tag{20}$$

where ϕ is the tangent angle of the beam, s is the arc length coordinate, $\bar{r}$ is a moment arm, and $\bar{F}$ is the end load. Subscript i refers to the node number, which we define as 1 at the location of F and n at the beam base. By starting at node 1 and repeatedly calculating the location of the next node up until n, Equation (20) provides an accurate, efficient, compact and easy-to-implement way of computing the shape of a beam due to an end load. Note that the generality of this method allows arbitrary inclination of the force, arbitrary variation of E and I along the length, and arbitrary inherent curvature of the beam (so long as the radius of curvature is at least 10 times the beam depth (i.e. the beam diameter in this case) at all nodes (Young and Budynas 2001)).

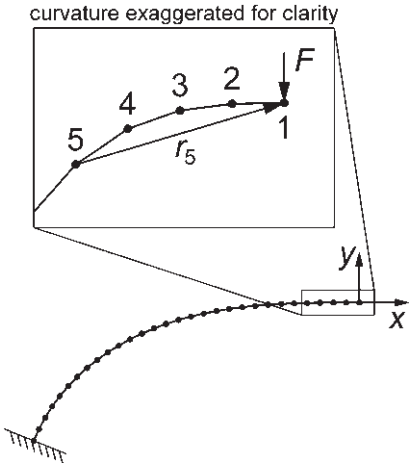

Fig. 10. Depiction of the numerical modeling process. The deflected shape of a cantilever beam with a concentrated end load F acting perpendicular to the beam's longitudinal axis can be found using a simple finite difference procedure depicted here. Only 30 beam nodes are shown for clarity, but a much larger number should be used for highly accurate results.

In this application the beam is straight and has constant E and I; therefore (20) is particularly straightforward to implement using a finite difference method. We assume that the friction between object and beam is negligible, making the force perpendicular to the beam's longitudinal axis at the contact point. Figure 10 depicts the process of computing the beam shape for a force F. The procedure starts by placing node 1 at $(0, 0)$ and node 2 at $(-\mathrm{d}s, 0)$, where $\mathrm{d}s = 1/(n-1)$ such that F acts at arc length $s_F = 1$ along the beam and the initial tangent angle $\phi_1 = 0$. Successive node locations are then found by looping through the following equations, starting at $i = 2$ and ending at $i = n - 1$:

$$\kappa_{i-1} = x_i \cdot F, \tag{21}$$

$$\phi_i = \phi_{i-1} - \kappa_{i-1} \cdot \mathrm{d}s, \tag{22}$$

$$x_{i+1} = x_i - \mathrm{d}s \cdot \cos\phi_i, \tag{23}$$

$$y_{i+1} = y_i - \mathrm{d}s \cdot \sin\phi_i. \tag{24}$$

Once the beam shape is computed, its base point is translated to the origin, and it is rotated about its base by angle $-\phi_{n-1}$ to orient it as shown in Figure 2. Note that EI has been assumed to be 1, meaning that F is effectively normalized by s_F^2/EI. Also note that (20) could alternatively be easily implemented using a numerical integration algorithm, such as the Runge–Kutta method.

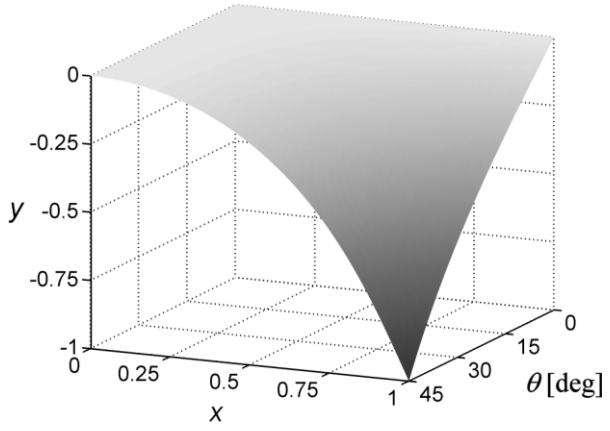

Fig. 11. A continuum of beam shapes. The shapes were computed by using the method depicted in Figure 10, up to $\theta_{\max} = 45^\circ$. Each beam length was normalized such that $d_x = 1$.

Repeating the above process for a succession of forces ranging from zero to $F_{\max}$ and storing the resulting beam shapes in a two-dimensional matrix amounts to pre-solving for all equilibrium shapes up to some maximum value of θ, $\theta_{\max}$ (which depends on $F_{\max}$). Figure 11 shows these results for $F_{\max} = 2.5$, which leads to $\theta_{\max} \approx 45^\circ$. A total of 10,000 nodes were used for high accuracy in computing the shapes, but only a subset of these points need to be stored in the look-up table because the underlying curves are smooth. Similarly, the beam changes in a very continuous manner as F increases, necessitating that only a relatively small number of shapes be stored. A table of size 100 × 100 provides excellent accuracy.

In general, one may wish to obtain the equilibrium shape, curvature or moment at the base, and contact angle γ based on various methods of query. In particular, (d_x, d_y), (r, θ), and (s_F, F, EI), where s_F is the actual location of the force, all independently provide sufficient information to reconstruct the entire shape of the beam by interpolating the look-up table and scaling the units to match those provided in the query.

A.3. Derivation of Translational Version of Sweeping Algorithm

The first modification involves the radial distance extraction component of the algorithm to reflect the translational movement of the whisker. Defining Δ_0 as the *pushing distance*, the translational analog of (1) can be found by substituting $\alpha_0 = \Delta_0 / r_0$ and solving for r_0, yielding

$$r_0 = \sqrt{3EI \frac{\Delta_0}{M_0}}. \tag{25}$$

Recalling (3)

$$\begin{bmatrix} d_{x,i+1} \\ d_{y,i+1} \end{bmatrix} = \begin{bmatrix} d_{x,i} \\ d_{y,i} \end{bmatrix} + \bar{\delta}_i + \overline{ds}_i,$$

again the task is to find expressions for $\bar{\delta}_i$ and $\overline{ds}_i$. The nominal deflection component $\bar{\delta}_i$ is simply opposite to the translational movement of the whisker:

$$\bar{\delta}_i = \begin{bmatrix} 0 \\ -\Delta_i \end{bmatrix}. \tag{26}$$

The longitudinal slip component $\overline{ds}_i$ is not influenced by the change from rotational whisker movement to translational, and remains the same. Equation (9) now becomes

$$\begin{bmatrix} d_{x,i+1} \\ d_{y,i+1} \end{bmatrix} = \begin{bmatrix} d_{x,i} \\ d_{y,i} \end{bmatrix} + \begin{bmatrix} 0 \\ -\Delta_i \end{bmatrix} + \left(M_{i+1} - M_{\delta,i}\right) \cdot \frac{\mathrm{d}s}{\mathrm{d}M_i} \cdot \begin{bmatrix} -\cos\left(\frac{3}{2}\theta_i\right) \\ \sin\left(\frac{3}{2}\theta_i\right) \end{bmatrix}. \tag{27}$$

References

Batista, M. and Kosel, F. (2005). Cantilever beam equilibrium configurations. *International Journal of Solids and Structures*, **42**(16–17): 4663–4672.

Clements, T. N. and Rahn, C. D. (2006). Three dimensional contact imaging with an actuated whisker. *IEEE Transactions on Robotics*, **22**(4): 844–848.

Dehnhardt, G., Mauck, B., Hanke, W. and Bleckmann, H. (2001). Hydrodynamic trail-following in harbor seals (*Phoca vitulina*). *Science*, **293**: 102–104.

Kaneko, M., Kanayama, N. and Tsuji, T. (1998). Active antenna for contact sensing. *IEEE Transactions on Robotics and Automation*, **14**(2): 278–291.

Kim, D. and Möller, R. (2007). Biomimetic whiskers for shape recognition. *Robotics and Autonomous Systems*, **55**(3): 229–243.

Krupa, D. J., Matell, M. S., Brisben, A. J., Oliveira, L. M. and Nicolelis, M. A. L. (2001). Behavioral properties of the trigeminal somatosensory system in rats performing whisker-dependent tactile discriminations. *Journal of Neuroscience*, **21**(15): 5752–5763.

Landau, L. D. and Lifshitz, E. M. (1986). *Theory of Elasticity*. Pergamon Press, Oxford.

Navee, S. and Elling, R. E. (1992). Equilibrium configurations of cantilever beams subjected to inclined end loads. *Transactions of the ASME Journal of Applied Mechanics*, **59**: 572–579.

Russell, R. A. (1992). Using tactile whiskers to measure surface contours. *Proceedings of the 1992 IEEE International Conference on Robotics and Automation*, Nice, France.

Scholz, G. R. and Rahn, C. D. (2004). Profile sensing with an actuated whisker. *IEEE Transactions on Robotics and Automation*, **20**(1): 124–127.

Schultz, A. E., Solomon, J. H., Peshkin, M. J. and Hartmann, M. J. (2005). Multifunctional whisker arrays for distance detection, terrain mapping, and object feature extraction. *Proceedings of the 2005 IEEE International Conference on Robotics and Automation*, Barcelona, Spain.

Solomon, J. H. and Hartmann, M. J. (2006). Robotic whiskers used to sense features. *Nature*, **443**: 525.

Solomon, J. H. and Hartmann, M. J. Z. (2008). Artificial whiskers suitable for array implementation: accounting for lateral slip and surface friction. *IEEE Transactions on Robotics*, **24**(5): 1157–1167.

Towal, R. B. and Hartmann, M. J. Z. (2008). Variability in velocity profiles during free-air whisking behavior of unrestrained rats. *Journal of Neurophysiology*, **100**(2): 740–752.

Tsujimura, T. and Yabuta, T. (1989). Object detection by tactile sensing method employing force/torque information. *IEEE Transactions on Robotics and Automation*, **5**: 444–450.

Ueno, N., Svinin, M. and Kaneko, M. (1998). Dynamic contact sensing by flexible beam. *IEEE/ASME Transactions on Mechatronics*, **3**(4): 254–264.

Wilson, J. and Chen, Z. (1995). A whisker probe system for shape perception of solids. *ASME Journal of Dynamic Systems, Measurement, and Control*, **117**: 104–108.

Young, W. and Budynas, R. (2001). *Roark's Formulas for Stress and Strain*. McGraw-Hill, New York.